Fabrication of Thin Film Nanocomposite (TFN) membranes modified with polydopamine coated metals/carbon-nanostructures for Desalination applications

Saif Al Aani[a], Alex Haroutounian[a], Chris J. Wright[b], Nidal Hilal[a*]

[a,]Centre for water Advanced Technologies and Environmental Research (CWATER), College of Engineering, Swansea University, Fabian Way, Swansea SA1 8EN, UK

[b] Biomaterials, Biofouling and Biofilms Engineering Laboratory (B3EL), The Systems and Process Engineering Centre (SPEC), College of Engineering, Swansea University, Fabian Way, Swansea SA1 8EN, UK

Abstract

Novel hybrid nanostructures (HNS) comprising of a mussel-inspired polymer coated metal/metal oxide (M/MO)–carbon nanotubes (CNTs), were successfully synthesised and used to fabricate Thin Film Nanocomposite (TFN) membranes for desalination applications. For comparison, four different M/MO (Aluminium oxide-Al_2O_3, Iron oxide-Fe_2O_3, Titanium dioxide-TiO_2 and Silver-Ag) nanoparticles (NPs) were *in situ* synthesized/loaded on the surface of CNTs, and the resultant HNS were further coated with a thin polymeric film of polydopamine (PDA)., An intermediate layer of HNS was then deposited between a PES substrate membrane and an interfacial polymerization (IP) process was carried out to render a polyamide (PA) thin layer on the intermediate layer. Both HNS and TFN were characterized using different characterization tools, including fourier transforms infrared spectroscopy (FTIR), zeta potential (ZP), X-Ray diffraction (XRD), raman spectroscopy, scanning electron microscopy (SEM), energy-dispersive X-ray spectroscopy (EDX), X-ray photoelectron spectroscopy (XPS), thermogravimetric analysis (TGA), surface hydrophilicity/hydrophobicity, and the performance of nanofiltration (NF) membranes were evaluated against monovalent and divalent salts solutions. The fabricated TFN-NF

membranes had higher performance in terms of their permeation characteristics compared to the thin film composite TFC membrane, while maintaining their selectivity against both monovalent and divalent salts solutions with only minor variation depending on the incorporated HNS used to prepare the TFN.

***Highlights*:**

Keywords: Thin film nanocomposite (TFN) membrane, Desalination, Polydopamine, metal/metal oxide nanoparticles, carbon nanotubes, hybrid nanostructure.

Corresponding author:
Email Address: n.hilal@swansea.ac.uk. (N. Hilal)

1 Introduction

Since the first Thin Film Composite (TFC) membrane was made by Cadotte [1], to the present day, a wealth of research has d targeted improving TFCs for a breakthrough in industrial membrane expansion for desalination applications. TFC, which is viewed as the "golden standard" in the membrane industry, is constructed by an interfacial polymerization of an organic phase-liquid phase system to form a thin (0.1–1µm) selective polyamide layer (PA) deposited on a microporous support substrate membrane. This standard polymeric membrane has been the topic of intensive research in recent years in order to bring about distinctive features to the TFC surface. Novel materials and surface modification methods have been adopted for designing what is believed to be the next generation of TFC membrane. One of the recent pragmatic approaches in this research has been achieved through revising the performance characteristics of TFC via imparting the specific characteristics of nanoscale materials (NMs) into the thin PA layer.

The recent concept "Thin Film Nanocomposite (TFN)", which was first reported in 2007 by Hoek [2], refers to the application of nanoscale materials within or at the top surface of a PA lay-

er. Since that time, a range of metal/metal oxides, zeolite and carbon based NMs have been reported in the literature, and reveal an enhancement in TFN membranes functions. The enhancement was not only targeted at the antifouling properties of nanocomposites, but also manifested outstanding capabilities to cope with the selectivity/permeability trade-off relationship [3]. These nano-based structures could be either added to the aqueous phase or to the organic phase during the fabrication reaction of the PA layer, or chemically bonded to the surface of TFC via bonding agents. However, gathering between a defect–free and stable PA layer is critical for long term durability and stable selectivity of any TFN membrane. Regardless of the role of monomer material, concentration and reaction time on the PA layer characteristics, other factors could considerably influence performance of TFN, such as type and size of fillers, degree of dispersion/aggregation and quantity incorporated into the PA layer, and polymer-filler compatibility. Size and type of nanofiller can affect the permeability characteristics of TFN, for instance big nanoparticle clusters or inappropriate alignment of nanotubes may act as a defect sites in the TFN layer and give rise to a lower selectivity [3, 4]. The relatively weak dispersion of hydrophilic NMs in non-polar solvents is another key problem for the approach in TFN formation steps where most research focuses on their dispersion in the aqueous phase [5]. Although considerable dispersion of surface modified NMs in the liquid phase canbe achieved, agglomeration of NMs is still unavoidable, especially at high loading weight. Nevertheless, lack of surface interactions between the PA matrix and NMs are more likely to result in leaching of NMs out of the PA thin film during the formation and/or filtration, affecting the selectivity and stability of the TFN membranes [3].

Currently, attempts are directed to modify the conventional IP process and/or to link diverse organic derivatives on NMs surface, aiming to revise their surface functionalization and promote their colloidal stability in various media. A new technique was introduced by Baroña and coworker to develop TFN membrane for low pressure RO membrane, where a single pass flow was used to incorporate aluminosilicate-single-walled carbon nanotubes (SWCNTs) in a PA layer [4]. Yin J. *et.al.,* have employed ethanol to facilitate the dispersion of graphene oxide (GO) in the TMC-hexane solution for PA thin-film layer formation [6]. While, Rajaeian *et.al.,* has utilized N-[3- (trimethoxysilyl)propyl] ethylenediamine (AAPTS) as a silane coupling agent to revise the surface characteristics of TiO_2 before addition to amine-aqueous solution for TFN/NF membrane fabrication [7]. Rajaeian *et.al.,* assumed that silane functional groups could minimize agglomera-

tion of nanoparticles (NPs)throughout by minimizing the probability of oxygen bridge bonds formation between TiO_2 NPs. One of the solutions for this is the use of dopamine (DA). DA as a mussel-inspired “bio glue” has been widely used for surface modification in a wide range of applications. Under an alkaline environment, DA can be self-polymerized to form a polymer-like coating layer of polydopamine (PDA) with great potential adhesive strength for a variety of organic and inorganic materials e.g. polymers, noble metals, oxides, semiconductors and ceramics [8]. PDA cannot only enhance the dispersion of nanofillers in aqueous solutions but also consolidate the surface interactions between PA matrix and NMs[9]. Lv Y. *et.al.*, identified that PDA can promote the interfacial stability between polymers and inorganic materials through acting as a bridge to chelate metal oxides for constructing inorganic films on various substrates [10].

In this research, instead of dispersing a nanofiller in the aqueous or organic phase aiming to embed them in the constructed PA layer, this introduces a thin hydrophilic intermediate layer of HNS between the substrate membrane and PA skin layer. This HNS comprised of metal/metal oxide NPs coated multiwalled carbon nanotubes (MWCNTs). Four different metal/metal oxide (Ag, Al_2O_3, Fe_2O_3 and TiO_2) were first deposited on the nanotube surfaces then coated with a PDA layer to get the final product.Next, a thin layer of HNS was deposited on a porous substrate membrane by vacuum filtration and the PA layer was adjusted to entirely cover and robustly fix the HNS interlayer in order to produce a defect-free TFN membrane. This method resulted in a low incorporation ofNMs and avoided their wastage during the TFN preparation. Vacuum pressure was applied instead of a rubber roller to remove excessive aqueous solution and to avoid any possible disruption or detachment of NMs layer that the rubber roller might cause during the preparation. This would also avoid any internal blockage of pores that could result during the PA formation, and lead to lower permeation characteristics. No appreciable amount of NMs would be wasted in order to incorporate a certain wt.% of NMs, as has been detected in the conventional TFN fabrication techniques. To the best of authors knowledge, no attempt has been made to use such novel hybrid nanostructure (HNS), comprising of CNTs-M/MO within the thin PA skin layer, and/or compared to the function of different types of HNS on the TFN characteristics.

2 Experimental

2.1 Materials and reagents:

All chemicals used in this work were used as purchased without further purification, except nanotubes. Raw MWCNTs were purchased from Chengdu Organic Chemicals Co. Ltd (China). Polyethersulfone (PES-Ultrason 6020P) flakes were kindly donated by BASF Co. Ltd (Germany). Nitric acid (HNO_3) 69% wt/v, iron(III) nitrate nonahydrate ($Fe(NO_3)_3.\ 9H_2O$), silver nitrate ($AgNO_3$), aluminium nitrate nonahydrate ($Al(NO_3)_3.9H_2O$), titanium(IV) butoxide ($Ti(OCH_2CH_2CH_2CH_3)_4$), absolute methanol and ethanol, Trizma-base and dopamine hydrochloride, and all related chemicals used for substrate membranes and TFN fabrication like Polyvinylpyrrolidone (PVP 40K), 1-methyl-2-pyrrolidinone (NMP) (≥99% purity), n-Hexane ≥95%, m-Phenylenediamine (MPD), 1,3,5-Benzenetricarbonyl trichloride (TMC), were purchased from Sigma-Aldrich (UK). Sodium chloride (Nacl), sodium sulphate (Na_2SO_4) and magnesium sulphate ($MgSO_4$) were analytical grade salts supplied by Fisher scientific (UK).

2.2 Synthesis of hybrid nanostructured materials

To eliminate amorphous carbon and trace metal catalysts, and to carboxylate the MWCNTs, 1000 mg of raw MWCNTs was dispersed in 200 ml HNO_3. The suspension was treatedfor 10 minutes in a bath sonicator, then refluxed under 120 °C for 48 hrs. Later, the solution was cooled down at room temperature, then diluted with DI water. Finally, the resultant precursor was passed through a 0.22 µm cellulose nitrate membrane, washed with DI water to neutralize the pH and dried in an oven at 80 °C overnight.

For decorating the nanotubes with metallic nanoparticles, 75 mg $Fe(NO_3)_3.\ 9H_2O$, 71.4 mg $Ti(OCH_2CH_2CH_2CH_3)_4$, 138.99 mg $Al(NO_3)_3.9H_2O$ and 40 mg $AgNO_3$ was individually added into 100 ml methanol and bath sonicated for one hour. Then, 100 mg of carboxylated nanotubes prepared earlier were added and sonicated for another 30-min with a tip sonicator to yield about 10 wt.% metal to the MWCNTs. Thereafter, the precursor was dried at 40 °C in a vacuum oven. Finally, to convert metal salt into metallic form on the surface of CNTs, each sample was calcinated in a tube furnace at 450 °C under inert conditions for 5 hours.

Coating the nanostructure with a thin layer of PDA was carried out using a bath sonicator to suspend 50 mg of each HNS sample in 100 ml Tris-HCl buffer (10mM and pH 8.5). About 75

mg dopamine was then added and stirred at 25 °C for 24 hr. After polymerization, the PDA coated nanotubes were washed several times to pH neutral. Finally, the product was dried under vacuum overnight. An example of the prepared HNS is presented in Figure 1.

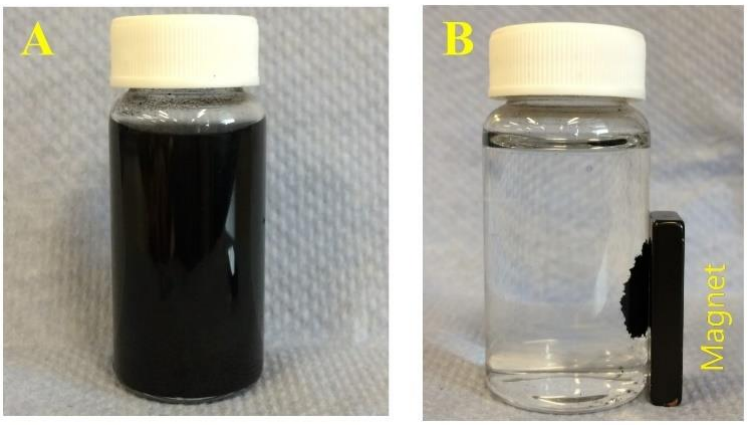

Figure 1: Photographic view of Fe_2O_3–CNTs nanocomposites: (A) dispersed in water, (B) their response to a magnetic field.

2.3 Fabrication of thin film nanocomposite (TFN)

Laboratory made PES/UF membranes were prepared by the classical wet phase inversion and used as a substrate for the polyamide layer polymerization. A more detailed fabrication description of the procedure is presented in a previous work [11]. Briefly, 14 wt.% PES and 2 wt.% PVP were dissolved in NMP at 50 °C overnight, untill a clear yellowish solution was achieved. The casting solution was then degassed for 1 hour under vacuum prior to casting. Next, membranes were casted on non-woven support (Ahlstrom-Hollytex$^{@}$ - grade:3329) using a thin film applicator with a clearance gap of 200 microns. Thereafter, the substrate was directly placed in a DI water coagulation bath at 20 °C for 30 minutes, washed several times, and stored in an air tight DI water container at 4 °C ready for further use.

TFC and TFN membranes were fabricated via interfacial polymerization on the membranes prepared earlier. For TFC membrane, a rectangular cut membrane was first clamped between a rectangle frame (20 cm X 5 cm) and substrate made from acrylic, and connected to a vacuum unit. About 50 ml of 2% MPD (w/v) in water solution was left in contact with the active mem-

brane's surface for two minutes, followed by applying a vacuum pressure to remove the excess solution. Then, 50 ml of 0.1% TMC in n-hexane (w/v) was reacted with the top surface of the MPD wetted substrate for 45 seconds. After the IP process, the TFC was rinsed with about 50 ml n-hexane to remove unreacted monomers, crosslinked in oven at 70 °C for 15 minutes, and finally stored in DI water prior to testing.

Except for one additional step, the same procedure was performed for the TFN fabrication. Following the clamping of the support membrane, a suspension of each PDA coated HNS was individually prepared and used to deposit 0.0025 mg/cm^2 on the support membrane by vacuum filtration, forming a very thin layer of HNS on the top surface. The MPD was then poured carefully to wet the deposited thin layer for 2 minutes. Then, vacuum pressure was applied again to remove excess solution from the surface and to wet the internal wall of pores. As mentioned in TFC procedure, TMC was then reacted with the amine solution for 45 seconds, rinsed with n-hexane, crosslinked at 70 °C, and stored in DI water ready for characterization.

2.4 Characterization

2.4.1 Fourier transforms infrared spectroscopy (FTIR)

To affirm the existence of functional groups on the acid modified MWCNTs and TFN membranes surface, a fourier transform infrared spectrophotometry (FTIR) (Spectrum 2-PerkinsElmer) was implemented. The transmittance spectra were recorded at room temperature from 500 to 4000 cm^{-1} with a resolution of 4 cm^{-1}.

2.4.2 Zeta potential

A universal dip cell kit (ZEN1002), as an accessory for Zetasizer nanoseries ZN (Malvern, UK), was used to determine the zeta potential (ζ) of raw MWCNTs, *f*-MWCNTs and HNS prior and after PDA coating. A concentration of 5 mg/L for each HNS in water was prepared individually and pH was titrated from 3-11, using 0.1 M HCL and 0.1 M NaOH. The zeta potential was then measured as function of pH, and the isoelectric point of each sample was determined.

2.4.3 X-Ray Diffraction (XRD)

XRD patterns were recorded on a Brüker d8 DISCOVER diffractometer with a Cu kα X-Ray source (λ = 0.15418 nm) and analysed using Match 2 software.

2.4.4 Morphological and elemental analysis

The surface roughness parameters were characterized using atomic force microscopy (AFM) t. A multimode AFM with a NanoScope IIIa controller (Bruker, USA) was used for this purpose. Scanning electron microscopy (SEM S4800- Hitachi, Japan) was used to observe the morphology, and energy dispersive X-ray analysis (EDX) attached to the SEM was implemented to provide quantitative representation for the elemental composition of various samples.

2.4.5 Raman spectroscopy

Raman spectroscopy as a non-destructive technique was applied to evaluate the graphitic structure, defects, ordered and disordered structures of HNS. The Raman spectra was recorded for samples on InVia™ Confocal Raman Microscope (Renishaw-UK) with a 532 nm excitation laser.

2.4.6 Thermogravimetric analysis (TGA)

Thermal gravimetric analysis (TGA) (TA Instrument-Q600SDT) was performed to determine the thermal decomposition behaviour of HNS, confirm the loading weight of metals on the surface of nanotubes and the presence of a PDA coating layer. An aluminium pan was filled with approximately 5 mg of HNS and placed inside the combustion chamber, then heated in the presence of air up to 900 °C (heating rate 10 °C /min and air flow rate 100 ml/min).

2.4.7 X-ray photoelectron spectroscopy (XPS)

Elemental composition and chemical state was further characterized by XPS analysis. An X-ray photoelectron spectrometer (Kratos, AXIS SUPRA-Japan), equipped with a monochromatic Al Kα as the radiation source, was used to identify the HNS from a range of 0-1200 eV. CasaXPS software was used for data analysis. A calibration of spectrum energy was carried out with respect to C1 peak, and binding energy (BE) set to 284.8 eV.

2.4.8 Surface hydrophilicity/hydrophobicity

Surface hydrophilicity/hydrophobicity of the TFC and TFN membranes was carried out by a sessile drop method using a VCAoptima contact angle instrument. 4 µl droplet of DI water was dropped down on a flat membrane's surface, and an image of the droplet was automatically captured to determine the contact angle measurement using VCA Optima XE software.

2.4.9 Performance evaluation of Nanofiltration NF membranes.

PWF and salts filtration experiments were conducted using a crossflow rig with an active membrane area of 12.6 cm^2. After adequate compaction time at a transmission pressure 1.2 MPa, the

pressure was reduced to 1.0 MPa and the DI water permeate flux recorded automatically every one minute using data collection software interfaced with an electronic balance. The automated software converted the permeate weight data received from the balance into a flux, and recorded the values on an excel spreadsheet for previously set membrane area and time intervals.

For the evaluation of NF performance. The inorganic salts concentration in feed solutions, including NaCl, Na_2SO_4 and $MgSO_4$ was kept at 2000 ppm. After the compaction with DI water, the permeate flux ($L/m^2.hr$) decline was recorded as described earlier for PWF, while rejection values (R%) of the membranes were determined by following equation:

$$R\% = 1 - C_p/C_f$$

Where C_p and C_f are the salt concentrations in the permeate and feed solution, respectively. A conductivity meter (Jenway-UK) was used to detect the salts concentration in the feed and permeate solution.

3 Results and discussion

3.1 Hybrid Nanoscale Structures.

3.1.1 FTIR Spectra evaluation of MWCNTs

The total reflection infrared spectra from 500 to 4000 cm^{-1} are shown in Figure 2.for raw, functionalized and PDA coated nanotubes. A clear enhancement in the partial oxidation of nanotubes was observed after treatment with concentrated HNO_3 where a number of functional groups, mainly hydroxyl (–OH) and carboxyl (–COOH), are generated after the acid treatment of r-CNTs. The FTIR spectra of r-CNTs did not reveal clear enough bands to be recognized. However, the broad well defined peak around 2994-3691 cm^{-1}, which is always presented for the nanotubes, is mainly attributed to the stretching mode of the (–OH) bond. The IR regions around 1665 cm^{-1} are ascribed to oscillation of –COOH groups, while the small peak at 1362 cm^{-1} is the O-H vibration bending of carboxyl acidic group [12]. The well-defined peak at 1060 cm^{-1} was correlated to the C–O stretching vibration. All these identified peaks confirmed the successful modification of r-CNTs with acidic functional groups. Comparing the IR spectra of CNTs and other HNS, a new peak ascribed to pure metal oxide NPs was observed between ~ 450-700 cm-1, depending on the M/MO type. Following the PDA coating, peaks at 1060 cm^{-1}, 1362 cm^{-1} and 1665

cm^{-1} have disappeared, and new peaks have emerged around 1272 cm^{-1} and 1572 cm^{-1} instead. These peaks are ascribed to C-O stretching vibration of Phenol and N-H vibration response of the amide II bands, respectively [13], which is considered as a confirmation of felicitous muscle inspired chemical packaging on the surface of HNS.

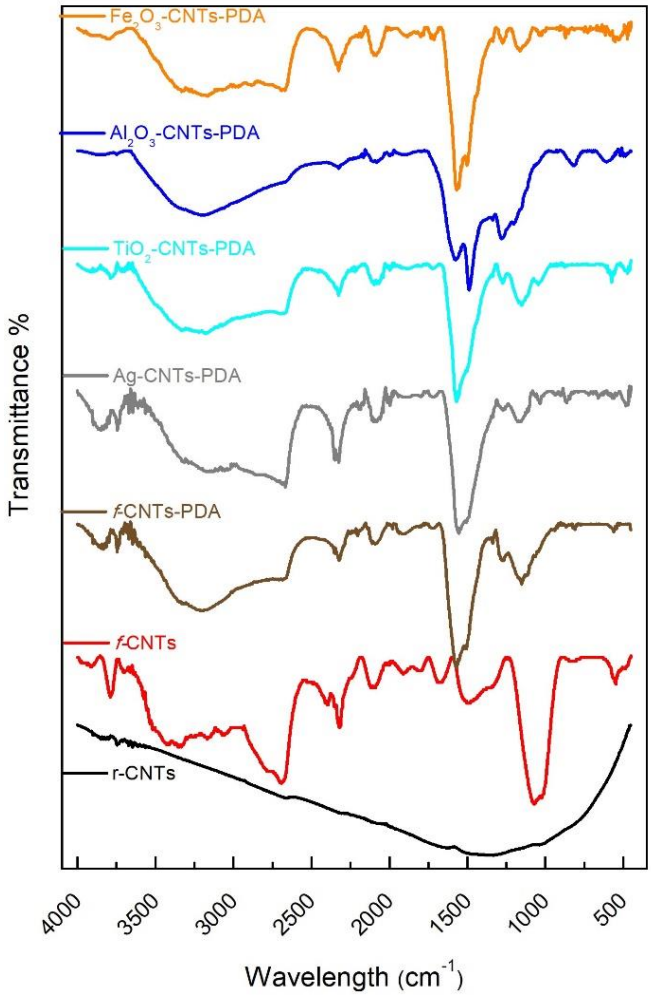

Figure 2: Fourier transform infrared spectroscopy (FT-IR) spectrum of r-CNTs, *f*-CNTs, *f*-CNTs-PDA and PDA coated nanocomposites.

3.1.2 Microscopic observation (SEM and EDX).

Surface morphology of nanotubes, prior and after metal/metal oxides decoration, was observed under SEM, as shown in Figure 3. No apparent destruction was identified in the structure of nanotubes following the refluxing process with concentrated HNO_3. A clear cylindrical nanostructure was shown as the bundles aligned together through the action of van der Waals

forces, Figure 3A. The only difference detected between the samples was their purity and oxygen content percent, as confirmed by the (EDX). Morphology of nanotubes, after decoration with metallic NPs is presented in Figure 3B - Figure 3E. No visible deposited metal/ metal oxides NPs were observed on the surface of the nanocomposites by SEM imaging, despite of the confirmed chemical composition results obtained from EDX. This was probably due to the small size of metal/metal oxides NPs packaged on the surface of MWCNTs. The EDX spectra confirmed the corresponding metal, oxygen and carbon for all HNS. The characteristic energy level for O_2 and C are located at 0.54 eV and 0.2 eV, respectively. While for the metals peaks were found to be at (3 eV), (0.35 eV and 4.5 eV), (1.5 eV) and (0.7 eV, 6.4 eV and 7.1eV) for Ag, Ti, Al and Fe, respectively.

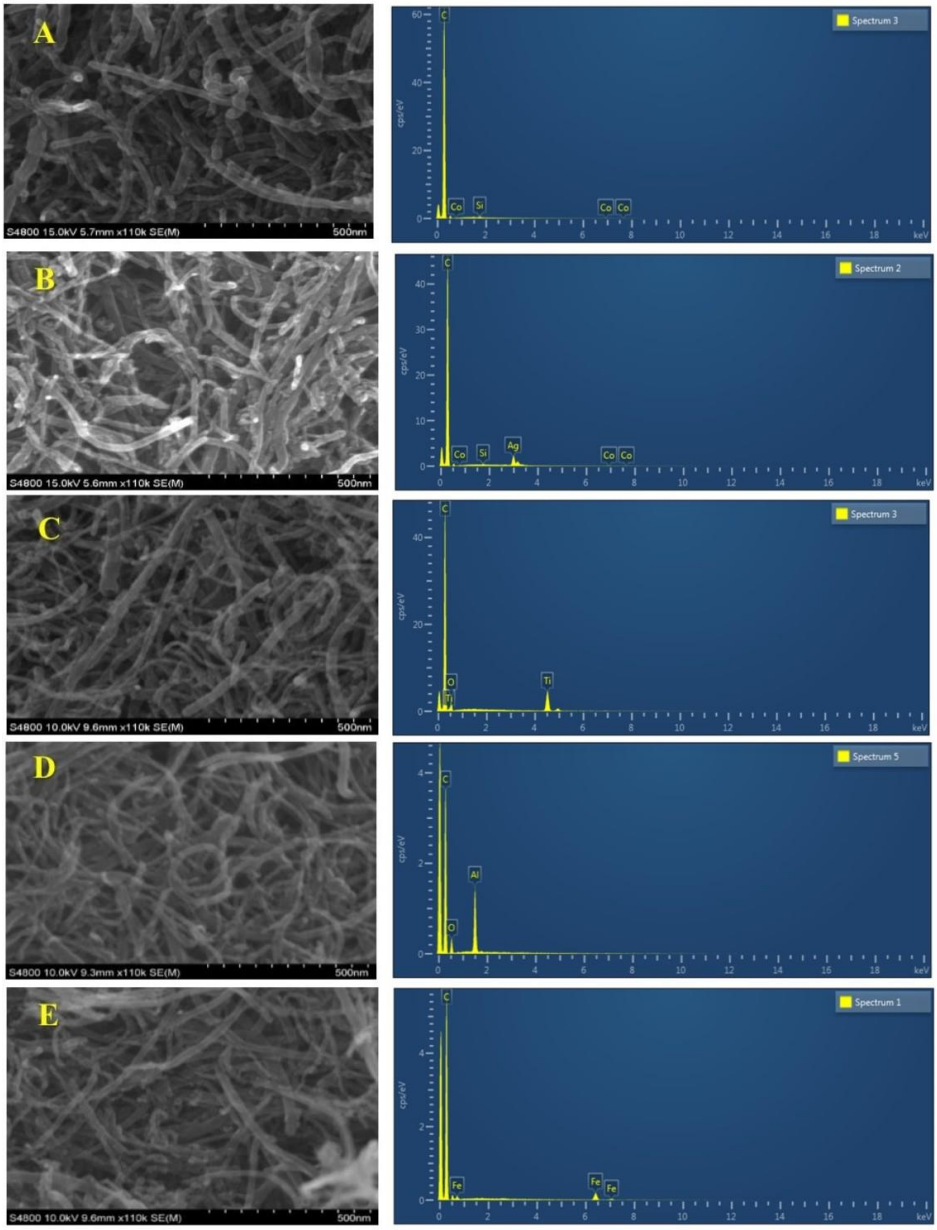

Figure 3: Microscopic images (Left) and composition analysis (Right) for (A) *f*-CNTs, (B) Ag-CNTs, (C) TiO_2-CNTs, (D) Al_2O_3-CNTs and (D) Fe_2O_3-CNTs.

3.1.3 X-Ray Diffraction analysis (XRD)

The XRD patterns of the crystalline structure of M/MO-MWCNTs nanocomposites are shown in Figure 4. All nanocomposites had XRD patterns with the distinctive two diffraction peaks at 42 and 26 that correspond to (100) and (002) reflections of the graphite layers' structure [14]. After decorating the nanotubes with AgNPs, another three peaks were observed at 64°, 44° and 38° that correspond to the (220), (200) and (111) reflections associated with Ag (0) as shown in Fig-

ure 4C. Since different phases of iron oxide (magnetite-Fe_3O_4, hematite-α-Fe_2O_3 and maghemite-γ-Fe_2O_3) have very similar XRD patterns, it's hard for the XRD technique to distinguish between them [15]. This scenario could be worse in the presence of another material to form a hybrid nanocomposite (NC). However, the existence of diffraction peaks at 32.5° (104), 50° (024) and 63° (300) could be deemed as a confirmation for α-Fe_2O_3 formation, rather than other iron oxide phases (Figure 4D). For the other HNS, no visible XRD peaks attributed to TiO_2 and Al_2O_3 were detected in the TiO_2 -CNTs and Al_2O_3-CNTs spectra (Figure 4E and Figure 4F). This could be due to the lower extent of the crystalline metals, compared to the crystalline CNTs, used to prepare these HNS, leading to shielding of the metal peaks by those of the nanotubes, and/or the TiO_2 XRD peaks in the nanocomposite could be overlapped by the nanotubes peaks since the main peaks position of TiO_2 at 25.4° is close to the main diffraction peak of the nanotubes at 25.9°. The opposite of these findings were reported by *Yu et.al*., astitaniium masked the nanotubes peaks when TiO_2 had a higher loading to that of nanotubes in the HNS [16]. Further characterization has been carried out to avoid the XRD limitations and assert the HNS composition/oxidation state.

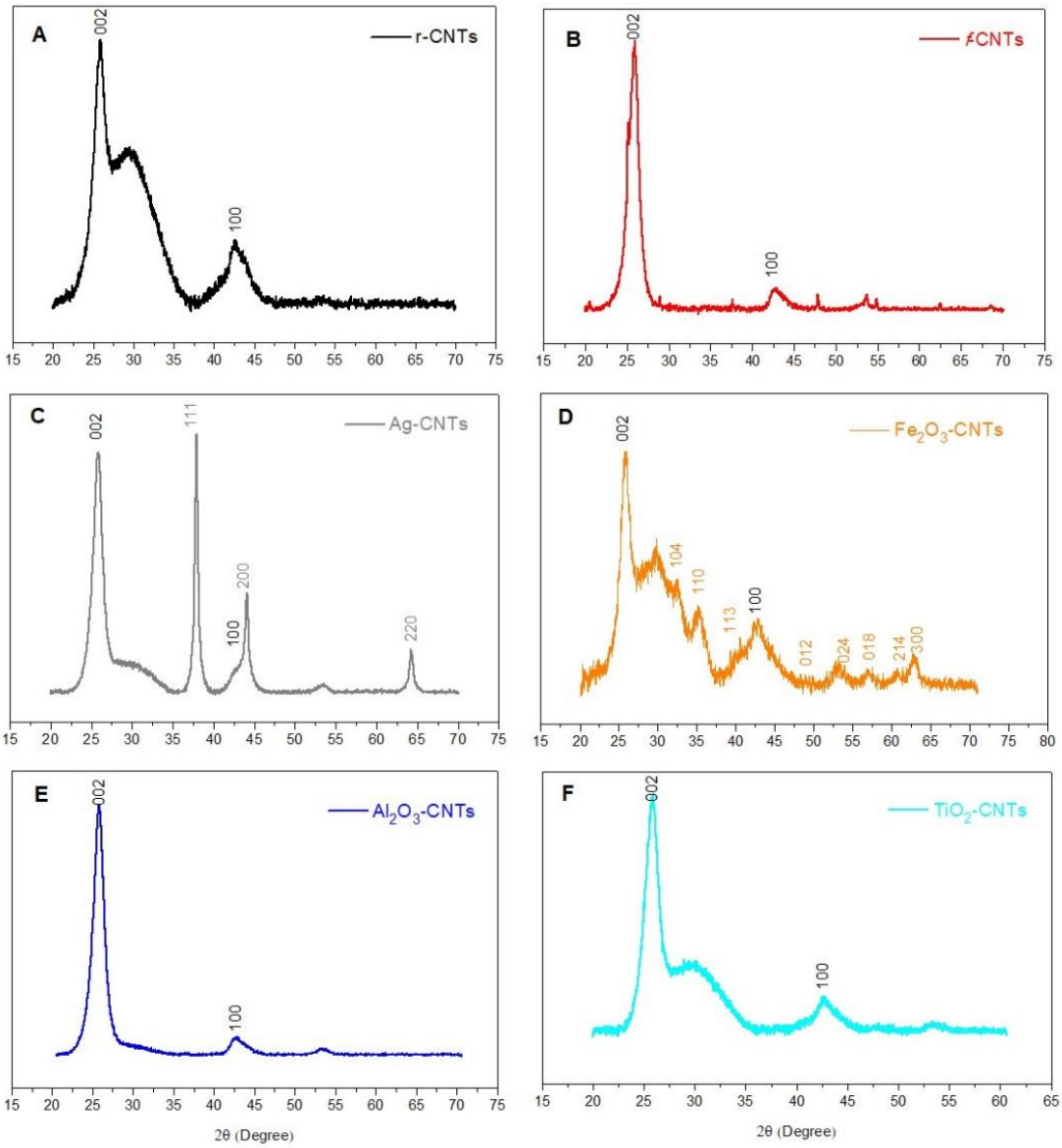

Figure 4: XRD patterns of (A) Ag-CNTs, (B) Fe_3O_4-CNTs, (C) Al_2O_3-CNTs, and (D)TiO_2-CNTs.

3.1.4 Raman spectroscopy

The structural changes, prior and after decorating the nanotubes with M/MO, were determined by Raman spectroscopy bands, Figure 5 (Right). All carbon nanotubes bands differentiated by Raman spectra were located between 1000-1700 cm^{-1}. The band denoted as (G-band) at 1572 cm^{-1} is ascoiated with the graphitic layers and is the characteristic feature of all sp^2 hybridized carbon allotropes. While the additional peak named as (D-band) at 1340 cm^{-1} refers to the defects

and disorder of the structure [17]. Following the acid treatment and the subsequent decoration step, some differences between the spectra have been highlighted;; a decrease in the G band intensity relative to the D band have been observed for *f*-CNTs and all other HNS. The intensity ratio between D band and G band (I_D/I_G) was used to determine the degree of disorder in the HNS samples. An increment in the I_D/I_G from 0.76 to 0.85 was observed, suggesting an increase in the defects and disorder on the nanotubes after processing with HNO_3 has been accomplished. Furthermore, presence of metal/metal oxides on the surface of nanotubes caused explicit changes in Raman scatter intensity, and the I_D/I_G were found to be 0.90, 0.85, 0.85, 0.92 for Fe_2O_3-CNTs, Al_2O_3-CNTs, TiO_2-CNTs and Ag-CNTs, respectively. Indicating that incorporating M/MO induced more defects and degree of disorder of the CNTs. Even though the change in the I_D/I_G ratio has been used as an indication for the attachment of metallic NPs on the surface of nanotubes [18], this change was not tangible after deposition of metallic NPs in this work. This could be due to the preferential growth of NPs on surface defects sites of nanotubes, resulting in a reduction in these structural defects, and leading to a small increase in the I_D/I_G ratio [19]. Moreover, different nanocomposites manifested a different morphologic I_D/I_G ratio, regardless if the same *f*-CNTs were used for later metal deposition. Probably, this disparity may be different from one metal to another depending on NPs size and distribution's homogeneity, when grown on surface defects of the nanotubes.

In Raman spectroscopy, different material phases can be distinguished, depending on their individual frequency, and elucidated as peaks. Figure 5 (Left) shows the Raman spectra of different metallic NPs loaded on nanotubes between 100 cm^{-1}-1000 cm^{-1}. The well-defined Raman peak of TiO_2 determined at 150 cm^{-1} is assigned to the main anatase vibration mode (E_g) of Titanium. Other Vibration peaks observed at 398 cm^{-1}, 505 cm^{-1}, 625 cm^{-1} represent (B_{1g}), (A_{1g}) and (E_g) suggesting that anatase phase is the main crystallite structure for the TiO_2 [20]. While the scattering peaks located at 216 cm^{-1} and 282 cm^{-1}, 393 cm^{-1} and 616 cm^{-1} in the Fe_2O_3 Raman spectrum are attributed to the vibration modes of α-Fe_2O_3 [21], which agreed with the suggested XRD results..

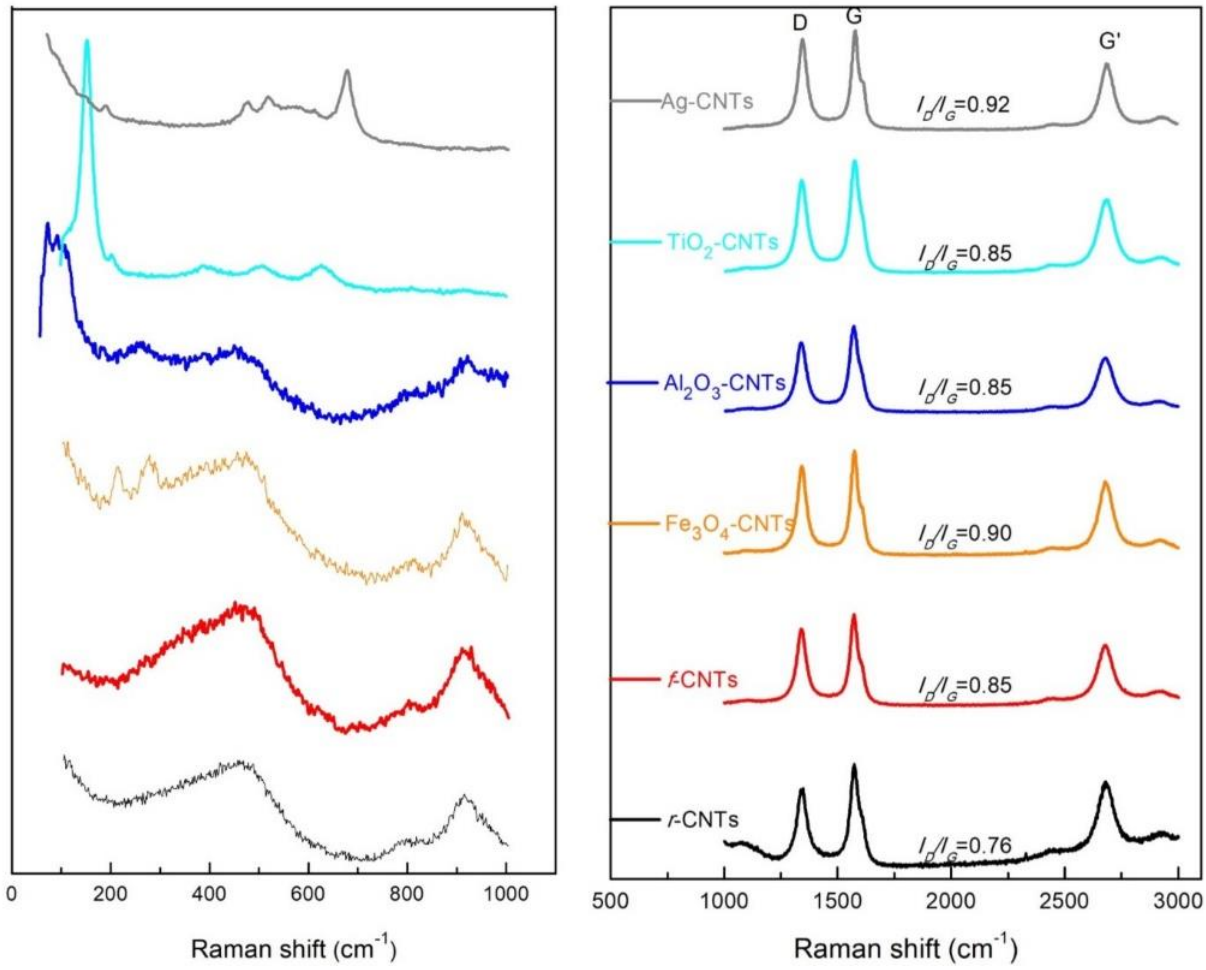

Figure 5: Raman spectroscopy results for pristine, functionalized and metal/metal oxides decorated MWCNTs.

3.1.5 X-ray photoelectron spectroscopy (XPS).

To reveal the chemical composition and oxidation state of the uppermost surface of HNS, a typical XPS survey scan has been implemented. As indicated in Figure 6A, the elemental composition of nanotubes, including carbon (C) and oxygen (O), were observed in scans of all samples. More detailed information on XPS spectra (C1s) are provided in Figure 6B. The photoelectron peak C1s, ascribed to the graphitic carbon on nanotubes, is located at 284.8 eV. and the other elemental characteristic peak (O1s) is located at 532 eV binding energy (BE) (Figure 6C). Following the acid treatment, a change in C1s and O1s has been observed indicating the degree of surface oxidation. The O/C ratio has increased from 7% to 9.65%, indicating more oxygen atoms are bounded to the *f*-MWCNTs according to XPS results. These results correlated with the in-

creased defects and disorders (I_D/I_G ratio) created on the nanotubes surface after acid treatment, which was determined by Raman spectra

The subsequent decoration of nanotubes with M/MO has generated novel peaks in the XPS spectra. The Fe_2O_3-CNTs spectrum, depicted in Figure 6D, illustrates the shape and position of peaks at 711.3 eV and 724.7 eV, and assigned to Fe $2p_{3/2}$ and Fe $2p_{1/2}$ of α-Fe_2O_3, respectively [22], with energy separation between the two spin orbit components (ΔBE =13.4 eV). In addition, there was a shake-up satellite peak situated at 719 eV, which is identified as the characteristic of Fe^{3+} in Fe_2O_3 [23]. The phase of TiO_2 was also verified by XPS survey spectra, Figure 6E. The core level BE 259.3 eV and 265.2 eV of Ti $2p_{3/2}$ and Ti $2p_{1/2}$ respectively, has indicated the formation of $Ti4^+$ in Titanium [24], with 5.7 eV splitting energy between them. While, formation of Al_2O_3 on the surface of nanotubes was asserted by the characteristic peak Al 2p detected at a binding energy position of 74.6 eV [25], see Figure 6F. In additon, the double peak (368.4 eV and 374.5 eV) in the Ag-CNTs XPS spectrum (Figure 6G) corresponds to Ag $3d_{5/2}$ and Ag $3d_{3/2}$ electronic states related to Ag^0 [26].

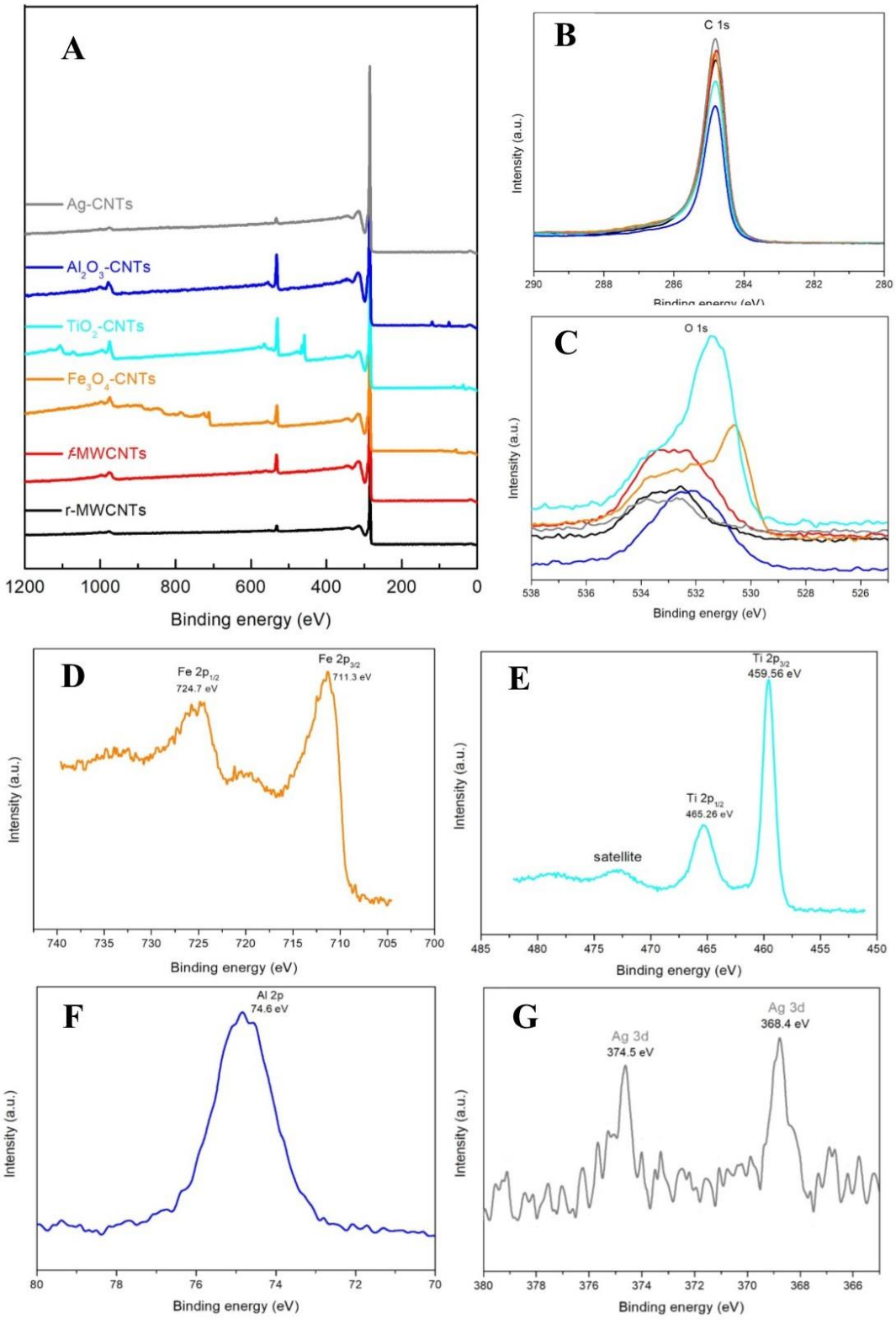

Figure 6**:** XPS spectra of CNTs and NC. (A) Full survey scan range from 0 to 1200 eV. (B) C1s region, (C) O 1s region. In addition to (D) Fe 2p region, (E) Ti 2p region, (F) Al 2p region and (G) Ag 3d region of HNS.

3.1.6 Thermal behaviour Analysis (TGA)

TGA analysis was conducted to illustrate the thermal decomposition behaviour of various samples, and to confirm the theoretical amount of M/MO and PDA loading weight used to coat the nanotubes. Considerable variation in the thermal properties was noticed under an oxidative environment for each metal, Figure 7 (Left). A gradual weight loss was detected for *f*-MWCNTs, before the significant loss at 547 °C commenced, this was ascribed to the decomposed organic moieties that manifested after the nanotubes acid treatment. Similarly, this wet loss was also observed for the other HNS, and could be due to the condensation reactions of metal-OH residual groups presented at the HNS materials [27]. In the meantime, deposition of Ag on the nanotube reduced the onset decomposition temperature to 309 °C, which was due to the oxidative catalytic ability of Ag that can catalyse, at low temperature, carbon nanotubes in the presence of O_2 [28]. However, presence of TiO_2 and Fe_3O_4 did not have any influence on the thermal properties of the MWCNTs, which were almost identical to that of *f*-MWCNTs. Unsurprisingly, this was not the case for the nanotubes coated with Al_2O_3, and the thermal decomposition temperature commenced at 635 °C due to the improved thermal stability of MWCNTs resulting from the synergy of alumina. Finally, the amount of M/MO, remaining after decomposition of nanotubes in the samples, has confirmed the theoretical loading level adopted in this research.

The extent of PDA grafting on *f*-MWCNTs and other HNS was evaluated by TGA analysis. The significant weight loss in the *f*-MWCNTs was between 547-673 °C, as illustrated in Figure 7(Left). At 547 C, the mass loss of *f*-MWCNTs was only 12%. While after coating with PDA, this weight loss reached 55%, suggesting that 43% of PDA was successfully loaded on the nanotubes via mussel inspired chemistry, Figure 7(Right). Similarly, the amount of grafted PDA on the surface of Fe_3O_4-MWCNTs, TiO_2-MWCNTs and Al_2O_3-MWCNTs was 34%, 40% and 45%, respectively. It should be noted that PDA slightly reduced the thermal stability of nanocomposites except that of Ag-MWCNTs. This was probably due tothe decomposition of PDA that lies within (200-500) °C [29], the final decomposition temperature of the nanocomposite has shifted from 400 °C to 545 °C, causing an improvement in thermal properties after PDA coating for Ag-MWCNTs samples only.

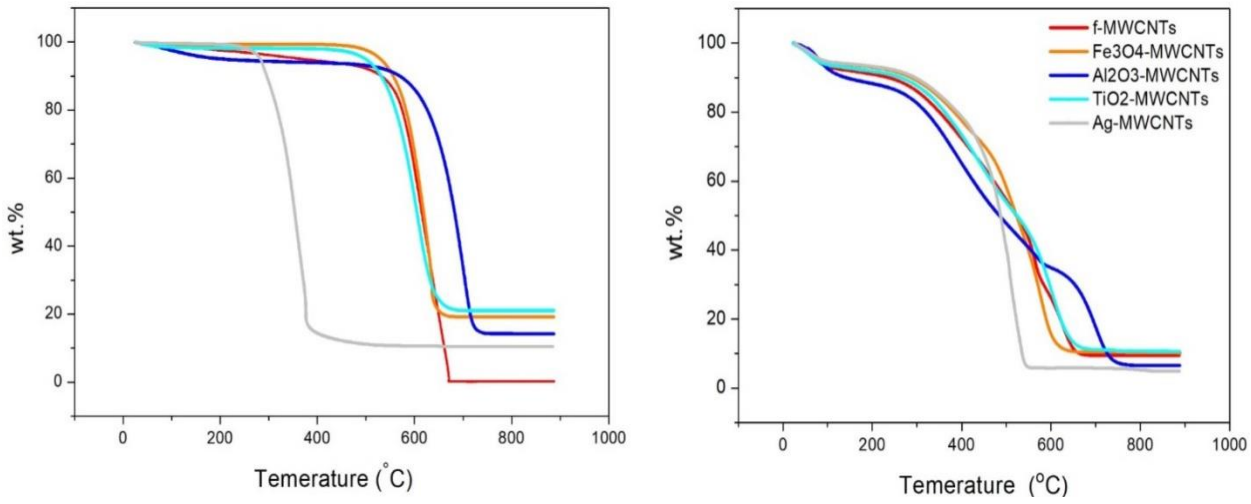

Figure **7**: TGA curves in air for nanocomposites (Left), and PDA coated nanocomposites (Right).

3.1.7 Zeta potential measurements

Zeta potential measurements were performed, as a function of pH (2.5-11), to evaluate the surface charge of *f*-MWCNTs, and the role of metal/metal oxides deposition and PDA coating layer on the zeta potential of the HNS.Significantly, acid treated nanotubes were negatively charged (-25 mV to -56 mV) for the entire pH range, where no isoelectric point (IEP) was detected even within a highly acidic environment, Figure 8(Left). The negatively functional groups are believed to act as nucleation sites for the later metal deposition on the surface of nanotubes [30]. However, decorating the *f*-MWCNTs with metal/metal oxides nanoparticles has shifted the zeta potential values, for all nanocomposites over the entire pH range, to more positive values. This was ascribed to the role of positively charged metal/ metal oxides nanoparticles that contributed to the total charge of the nanocomposite structures [28]. Moreover, coating the nanocomposites with PDA caused supplemental charge reversal especially in an acidic environment (below pH 5.5), and a clear shift in the IEP was observed toward a higher pH value for all PDA coated HNS, Figure 8(Right). This observation was due to the protonation of indole or indoline groups of PDA, which tends to neutralize the negative charge of HNS [31]. At higher pH (pH>6), all HNS commence to feature negatively charged surfaces.

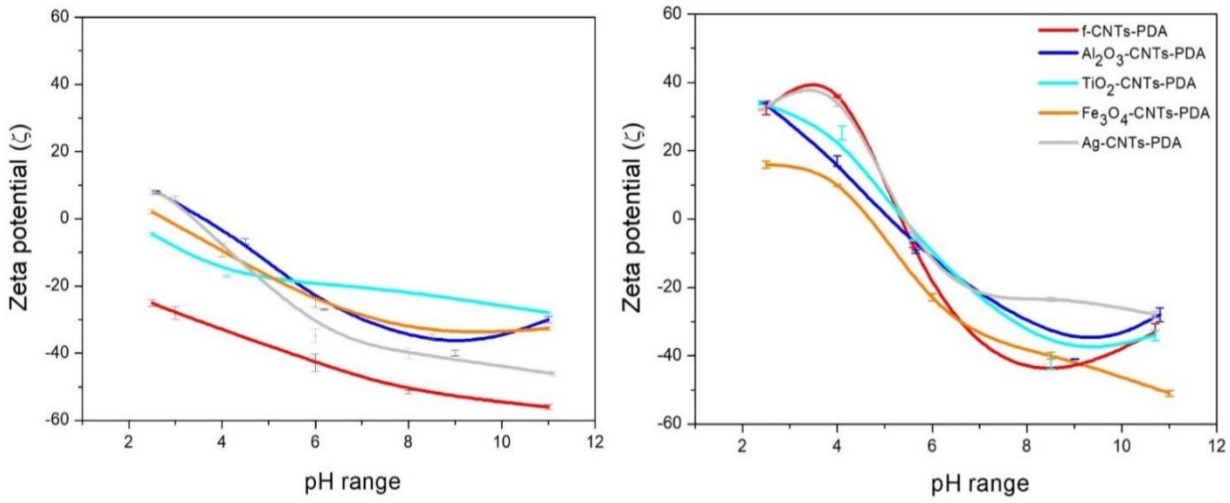

Figure 8: Zeta potential measurements as a function of pH, for; nanocomposites (Left), and PDA coated nanocomposites (Right).

3.2 Thin film nanocomposite membranes

3.2.1 FTIR

The chemical structure of the PES substrate, TFC and TFN membranes skin layer were verified by FTIR, as shown in Figure 9. Several peaks, associated with PES membrane, were observed around 1099 cm^{-1}, 1148 cm^{-1}, 1240 cm^{-1}, 1337 cm^{-1}, 1485 cm^{-1} and 1578 cm^{-1}, and correspond to C–O stretching, O=S=O symmetric stretching, aromatic ether, O=S=O asymmetric stretching, C=C stretching and benzene ring, respectively. More precisely, peaks found at 1485 cm^{-1} and 1578 cm^{-1} are the main characteristics of PES membrane material [32]. Following the interfacial polymerization of the PA layer, the IR spectra of TFC contained a novel peak around 1666 cm^{-1}. This peak is assigned to amide I band, a characteristic of C=O bonds of an amide group. In addition, there was alsoa more intense peak at 1578 cm^{-1} assigned to amide II band for N–H [4]. However, introducing the HNS as interlayers between the PES substrate and thin PA layer has influenced the intensity of some peaks (e.g. 557 cm^{-1},1485 cm^{-1}, 1578 cm^{-1} and 1710 cm^{-1}). The boosted intensity of the peak situated at 1710 cm^{-1}, was mainly due to C=O stretching vibration from –COOH groups of HNS [33]. Moreover, the formation of amide bands was also influenced in all TFN types.

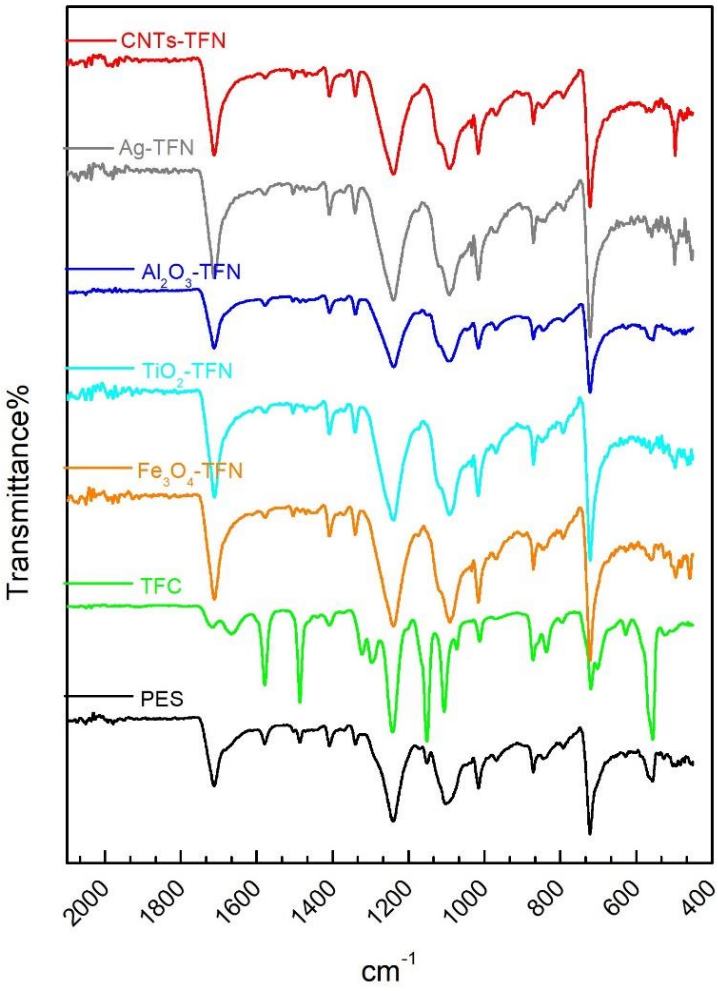

Figure 9: FT-IR spectra of the synthesized PES, TFC and TFN membranes.

3.2.2 Morphology of TFN membranes

The surface and cross sectional morphology of TFC and TFN membranes were observed by FESEM, as presented in Figure 10. The SEM surface images had the typical leaf-like structure of the PA layer. No explicit variation could be seen between TFC and TFN, which indicates that the PA layer has entirely covered the HNS interlayer, Figure 10A-10F(Left). While the cross-section images of all NF membranes have two distinct morphologies; the PA skin layer and the supporting PES substrate. The observed thickness of the PA thin-film layer in TFC membrane was ranging from 225 nm to 245 nm, while the active layer of all other TFN had a higher thickness (340 ±50 nm) comparedto that of TFC membrane. This augmentation in the thickness has been correlated to the existence of an HNS intermediate layer, which can absorb and store the

aqueous MPD solution to facilitate the subsequent interfacial polymerization process [33]. As depicted in Figure 10A-10F (Right), the presence of HNS was not conspicuous in the SEM cross-section images. This could be ascribed to the low contrast between HNS and the PA thin film, especially if they were wrapped within the PA polymeric matrix., It's believed herein that the interlayer was built up inside the PA matrix, and the PA forming monomers were penetrated, via the applied vacuum, through the HNS interlayer to attach the PES membrane surface and internal pores walls in order to anchor the thin film on the PES substrate.

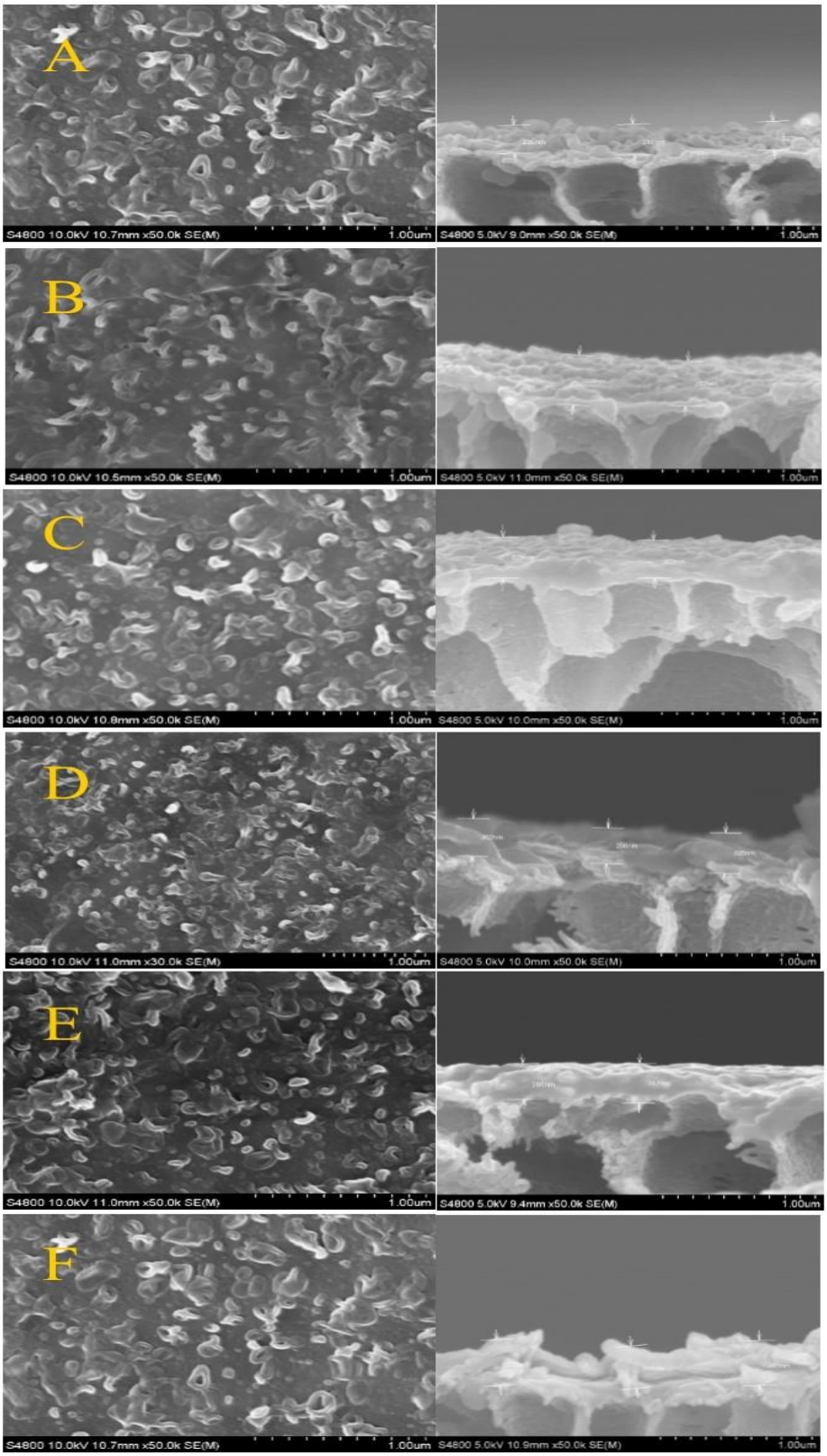

Figure 10: SEM surface images (Left) and cross-section (Right) for; (A) TFC, (B) f-CNTs-TFN, (C) Ag-TFN, (D) Al_2O_3-TFN, (E) Fe_2O_3-TFN, (F) TiO_2-TFN

3.2.3 Atomic force microscope (AFM).

AFM tapping mode 3-D images illustrating the surface topography of TFC and TFN are presented in Figure 11. A clear “leaf-like folds” structure, linked to the PA layer formation, can be observed on the surface of TFC membrane, Figure 11A. Meanwhile, introducing the intermediate layer of PDA coated HNS, to form TFN membranes, has changed the structure, where a combination of “leaf-like” and “ridge-to-valley” structure can be observed, Figure 11B-Figure 11F. This could be due the interruption of nanostructures on the growth of “leaf-like” structure during the polymerization reaction [6]. Moreover, the surface roughness parameters have been improved upon the addition of HNS, compared to bare TFC membrane. This enhancement in TFN surface morphology smoothness is more likely to be attributed to the well distributed HNS intermediate layer. Indeed, this provides not only a robust mechanical support but also a smooth and homogenous platform for the subsequent IP process. All roughness parametersroot mean square roughness-R_{ms}, root average arithmetic roughness-$R_{a,}$ and ridge to valley distance-$R_{max}$are summarized in Table 1.

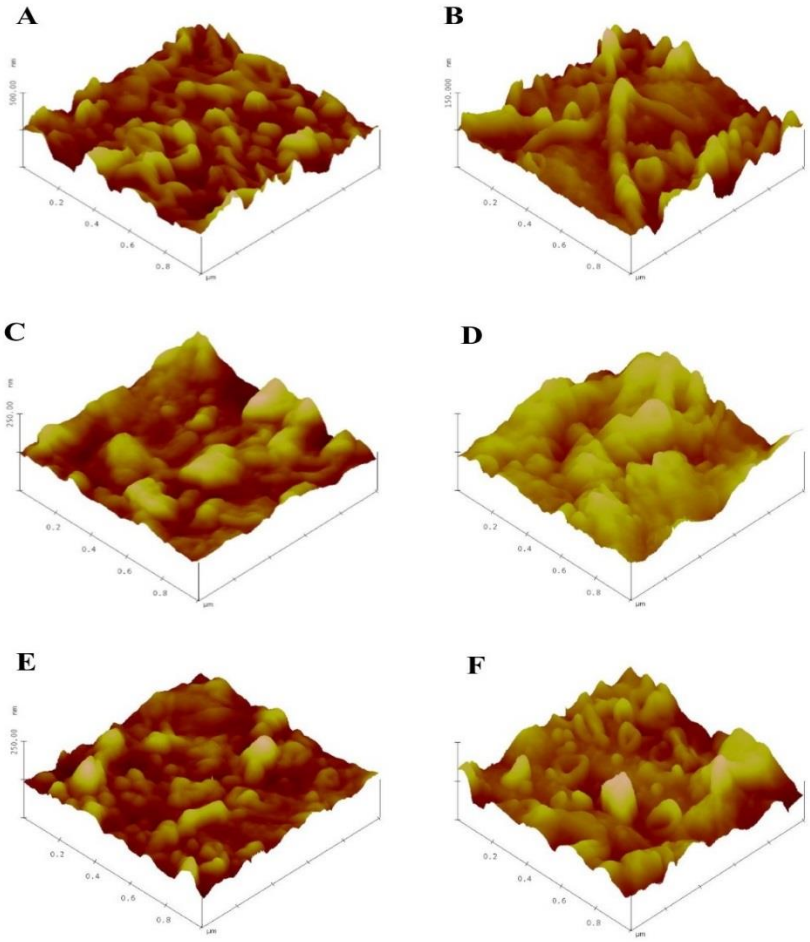

Figure 11: Three-dimensional-AFM images (5µm x 5 µm) of; (A) TFC, (B) *f*-CNT-TFN, (C) Al_2O_3-TFN, (D) Fe_2O_3-TFN, (E) TiO_2-TFN and (F) Ag-TFN.

Table 1: Average surface roughness parameters of TFC and TFN membranes

Membrane	R_{ms} (nm)	R_a (nm)	R_{max} (nm)
TFC	33.689	26.792	241.07
f-CNTs-TFN	13.196	10.268	110.46
Al_2O_3-TFN	15.395	11.974	93.135
Fe_2O_3-TFN	21.662	16.783	194.53
TiO_2-TFN	13.78	10.511	94.717
Ag-TFN	20.303	15.414	151.58

3.2.4 Static contact angle and hydrophilicity measurements.

Contact angle measurements were carried out to determine the role of PDA coated HNS incorporation on surface hydrophilicity/hydrophobicity of NF membranes. A noticeable decrease in the water contact angle (WCA) values were detected upon incorporating the nanostructures for all TFN membranes, as presented in Figure 12. The WCA of the bare TFC (57.5°) reported in this work was slightly lower than values ~ (60° -75°) reported in the literature for a PA skin layer. Wherein, disparate fabrication conditions (concentration of monomers, reaction time and support MF/UF characteristics), could result in some variation not only in the WCA values but also the overall characteristics of TFC membranes. The WCA of *f*-CNTs-TFN membrane, prepared with PDA coated *f*-MWCNTs, declined to 54° ,compared to that of TFC membrane. This decrease is suggested to be caused by the hydrophilic PDA and CNTs moieties in the TFN. In addition, presence of M/MO NPs on the surface of CNTs further diminished the average WCA values of TFN membranes by ~10° approximately, which was found to be 46°,46.2°, 43° and 47.6° for Al_2O_3-TFN, TiO_2-TFN, Fe_2O_3-TFN and Ag-TFN membranes, respectively.

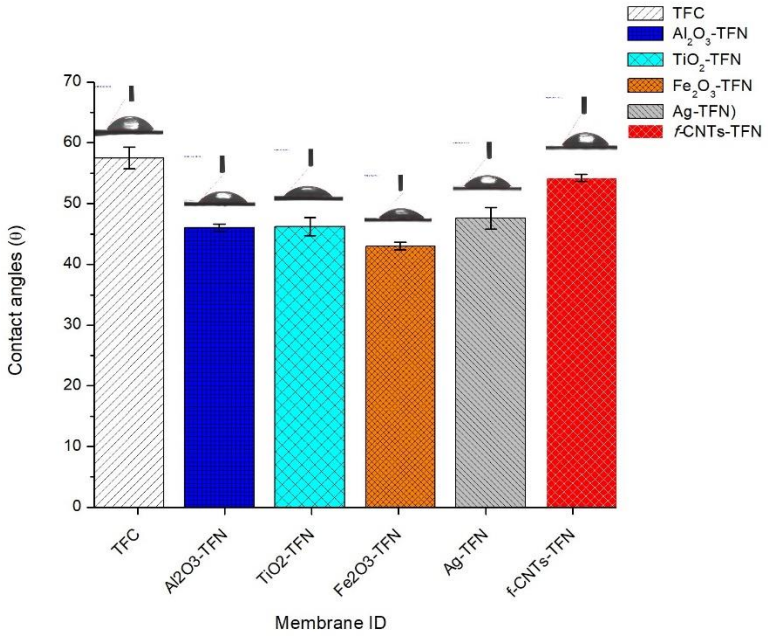

Figure 12: Static contact angle measurements of TFC and TFN membranes.

3.2.5 Performance evaluation of TFN.

The water permeation and separation characteristics for TFN membranes, synthesized with different types of M/MO-MWCNTs hybrid nanostructures under identical conditions, werecompared with that of TFC membrane. A representative monovalent (Nacl), divalent (Na_2SO_4 and $MgSO_4$), and a mixture of the three salts has been used for the separation's evaluation (Figure 13).

A clear enhancement was observedin the water permeability characteristic of all TFN, compared to that of the TFC membrane. Under 0.1 MPa applied pressure, the pure water flux (PWF) of TFN membrane, made with *f*-CNTs layer, was almost double (10.5 ± 0.2 L/m^2.hr) compared to that for to the TFC membrane (5.4 ± 0.1 L/m^2.hr). In addition, a further increase to 11.6 ±0.15 L/m^2.hr in PWF was observed with Ag-TFN membrane, while it had the lowest value (9.6 ±0.1 L/m^2.hr) for TiO_2-TFN. This substantial flux improvement exhibited by TFN membranes is more likely to be caused by the imparted hydrophilic nature of PDA and HNS synergy on the PA skin layer, facilitating the solubilisation and diffusion of H_2O molecules through the thin film. However, it should be noted that a membrane's permeability is a complex matter, and cannot be attributed to the hydrophilic nature of the nanostructured interlayer only, as other factors like surface roughness, charges and pore size/porosity may also contribute. The variation in PWF recorded was in the following order for Al_2O_3-TFN> Ag-TFN> *f*-CNTs-TFN> Fe_2O_3-TFN> TiO_2-TFN> TFC membrane.

In regard of single salt separation, a negligible loss in monovalent salts rejection was observed for all TFN comparing to TFC, where all NF membranes rejection factors were ranging between 92.60% to 93.67%, except that of Ag-TFN (91%), Figure 13A. While, 99.44 % and 97.15 % rejection was obtained by TFC membrane for the divalent salts, Na_2SO_4 and $MgSO_4$, respectively. Unsurprisingly, this was expected as typical negatively charged PA-TFC membranes have higher repulsion to divalent sulphate anions (SO_4^-) than mono valent chloride anions (Cl^-) due to Donnan-exclusion effects alongside the molecular sieving mechanism [34]. TFN membranes exhibited a higher potential for SO_4^-anions separation than Cl^-as well, but an explicit reduction in their divalent salts selectivity was noticed compared to TFC membrane, mainly for Na_2SO_4, Figure 13B and Figure 13C. This could be attributed to the shift observed on the zeta potential values of nanotubes after coating with positively charged M/MO and PDA to form the HNS, Figure 8. Indeed, some positive charges have been rendered on the TFN surface if com-

pared with the TFC, and this lowered the intrinsic negative charges of PA, as reported by Y. Lv *et. al*. [10]. Du and Zhao indicated that selectivity of positively charged NF can be dissimilar to that of negatively charged NF membranes, wherein positively charged TFC membranes can have higher rejection to Cl^- than SO_4^-[35]. Consequently, ionic transport and retention performance of NF membranes might reflect their charge characteristics. Therefore, in the present research the zeta potential of the surface of TFN-NF membranes may have led to some discrepancy in the rejection behaviour of the NF membranes., The flux decline during the single solute separation was in the order of Nacl >$MgSO_4$ >Na_2SO_4, respectively. While for the ternary salt filtration, the selectivity and the permeate flux decline were found to be somewhere in the middle for the identical mole fractions of each individual salt used in the filtration experiments, Figure 13D.

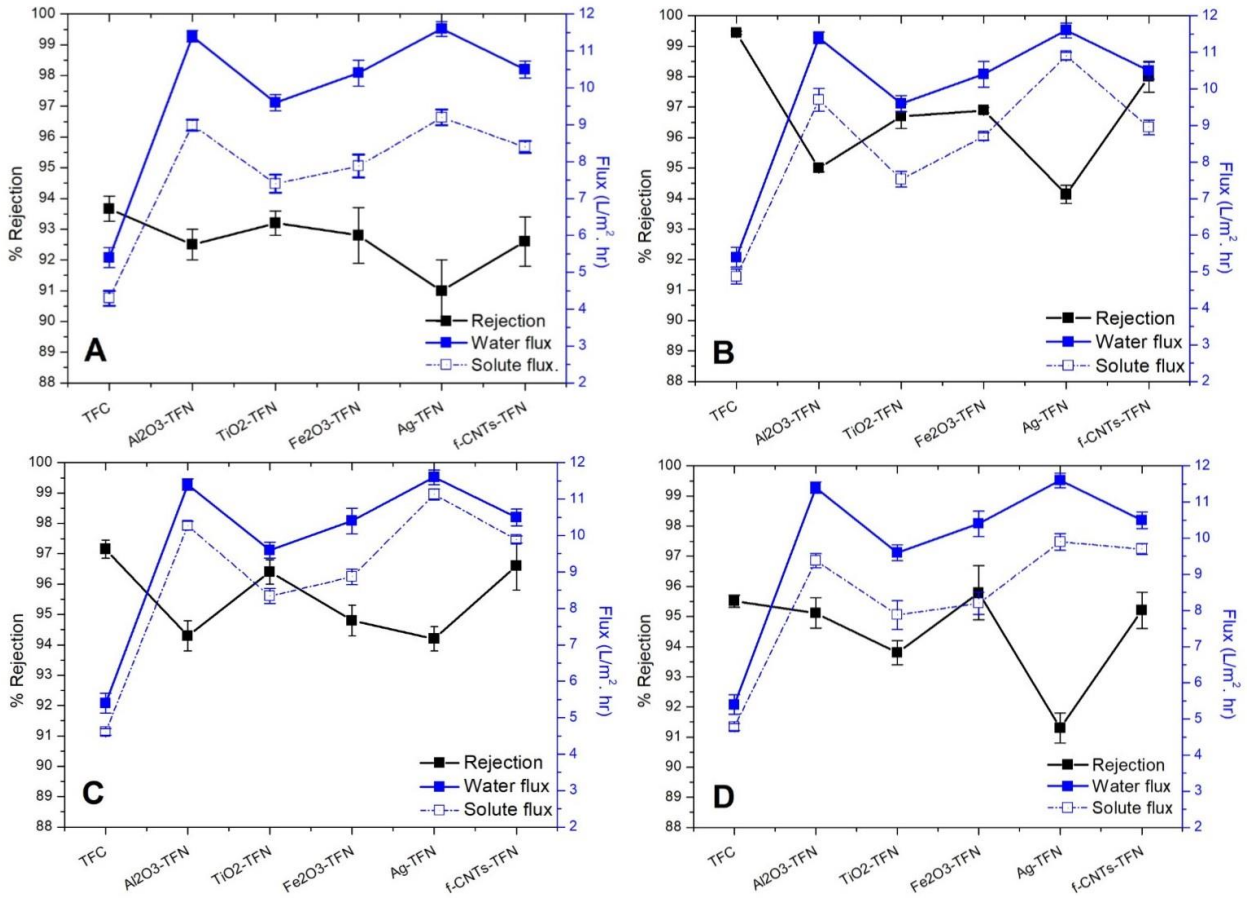

Figure 13: Separation, pure water and solute permeation of NF membranes against;(A) Nacl, (B) Na_2SO_4, (C) $MgSO_4$ and (D) ternary salt solution

The similar separation values indicate a successful construction of PA layer on the HNS intermediate layer without causing any defect on the skin layer of TFN. It should be noted that alignment of HNS interlayer on the PES substrate is crucial to facilitate the defects free PA layer construction process. Since their internal diameters are much higher than that of the selective PA skin layer, it's believed that any unaligned or/and uncovered nanotubes could act as channels for salts passage as well. In addition, it is critical to ensure a high stability in practical applications, through establishing a strong interfacial adhesion between the nanostructures layer and the PA on one side, and guarantee a firm interfacial adhesion with the PES substrate surface from the other side, so as to avoid any possible peeling of nanocomposite layer under cross-flow and high pressure conditions [33]. This can be achieved through controlling the deposited HNS layer thickness, pore size and roughness of substrate membrane, monomer concentration, reaction time and cross-linking conditions. Any increase in the concentration of HNS above the limit used in this work (0.0025 mg/cm^2) was found to cause further increase in the HNS interlayer thickness, that can act as a separator between the PA and PES substrate rather than strengthening the nanostructure. Indeed, Figure 14 shows a membrane that peeled of and couldn't survive the cross-flow conditions (high pressure and flow rate) used during the filtration experiments,

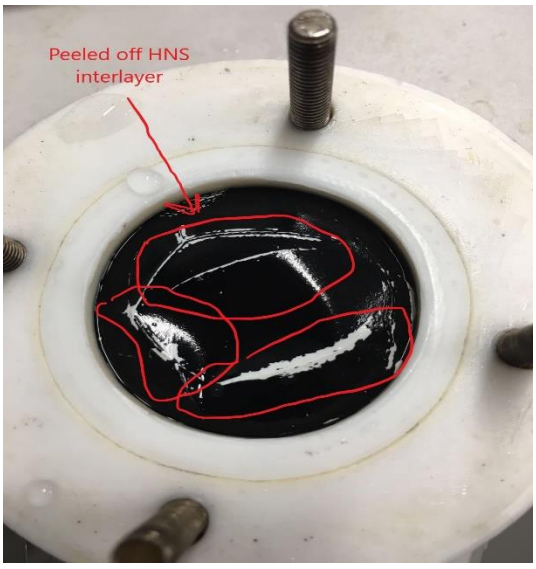

Figure 14: Peeling of the PA-HNS thin film layer under cross-flow conditions.

4 Conclusions

Novel TFN membranes for desalination applications were developed in this work, based on the fabrication and design of novel HNS. The characterization tools have quantitatively and qualitatively identified the fabricated HNS, where the composition of M/MO, their crystalline structure, thermal behaviour, surface charge alteration, oxidation states and PDA loading content have been determined. These were in turn assessed in terms of performance of the fabricated TFN membranes when introduced as an intermediate layer to revise their surface characteristics. Nearly double the PWF was obtained from TFN membrane compared to that of TFC membrane, without affecting the permeability/selectivity trade-off relationship. In addition, higher than 90% and 94% removals were achieved for monovalent and divalent salts, respectively. Indicating that NF membranes have been fabricated, that are capable of treating various salts at comparable level. The design of defect-free and mechanically stable PA layer on the HNS supported PES substrate where found to be contingent on the interlayer thickness. In summary, this enhancement in the surface characteristics of TFN membranes was attributed to the introduced hydrophilic intermediate layer masked by the PA. Thus, mussel-inspired coated HNS and their incorporation into TFC membranes have great potential in the design of NF membranes.

Acknowledgment

The Higher Committee for Education Development in Iraq (HCED) is kindly acknowledged for providing a Ph.D. scholarship to Saif Al Aani.

Nomenclatures

TFN	Thin film nanocomposite
HNS	Hybrid nanostructure
M/MO	Metal/Metal oxides
CNTs	Carbone nanotubes
PA	Polyamide
Al_2O_3	Aluminium oxide
Fe_2O_3	Iron oxide
TiO_2	Titanium dioxide
Ag	Silver
NPs	Nanoparticles
PDA	Polydopamine

References

[1] J.E. Cadotte, R.J. Petersen, R.E. Larson, E.E. Erickson, A new thin-film composite seawater reverse osmosis membrane, Desalination 32 (1980) 25-31.

[2] B.-H. Jeong, E.M. Hoek, Y. Yan, A. Subramani, X. Huang, G. Hurwitz, A.K. Ghosh, A. Jawor, Interfacial polymerization of thin film nanocomposites: a new concept for reverse osmosis membranes, Journal of Membrane Science 294 (2007) 1-7.

[3] W. Lau, S. Gray, T. Matsuura, D. Emadzadeh, J.P. Chen, A. Ismail, A review on polyamide thin film nanocomposite (TFN) membranes: history, applications, challenges and approaches, water research 80 (2015) 306-324.

[4] G.N.B. Baroña, J. Lim, M. Choi, B. Jung, Interfacial polymerization of polyamide-aluminosilicate SWNT nanocomposite membranes for reverse osmosis, Desalination 325 (2013) 138-147.

[5] H. Wu, B. Tang, P. Wu, MWNTs/polyester thin film nanocomposite membrane: an approach to overcome the trade-off effect between permeability and selectivity, The Journal of Physical Chemistry C 114 (2010) 16395-16400.

[6] J. Yin, G. Zhu, B. Deng, Graphene oxide (GO) enhanced polyamide (PA) thin-film nanocomposite (TFN) membrane for water purification, Desalination 379 (2016) 93-101.

[7] B. Rajaeian, A. Rahimpour, M.O. Tade, S. Liu, Fabrication and characterization of polyamide thin film nanocomposite (TFN) nanofiltration membrane impregnated with TiO 2 nanoparticles, Desalination 313 (2013) 176-188.

[8] X. Zhang, G. Zeng, J. Tian, Q. Wan, Q. Huang, K. Wang, Q. Zhang, M. Liu, F. Deng, Y. Wei, PEGylation of carbon nanotubes via mussel inspired chemistry: preparation, characterization and biocompatibility evaluation, Applied Surface Science 351 (2015) 425-432.

[9] Y. Lv, Y. Du, W.-Z. Qiu, Z.-K. Xu, Nanocomposite Membranes via the Codeposition of Polydopamine/Polyethylenimine with Silica Nanoparticles for Enhanced Mechanical Strength and High Water Permeability, ACS applied materials & interfaces 9 (2017) 2966-2972.

[10] Y. Lv, H.-C. Yang, H.-Q. Liang, L.-S. Wan, Z.-K. Xu, Novel nanofiltration membrane with ultrathin zirconia film as selective layer, Journal of Membrane Science 500 (2016) 265-271.

[11] S. Al Aani, V. Gomez, C.J. Wright, N. Hilal, Fabrication of antibacterial mixed matrix nanocomposite membranes using hybrid nanostructure of silver coated multi-walled carbon nanotubes, Chemical Engineering Journal (2017).

[12] F. Moraes, M. Cabral, L. Mascaro, S. Machado, The electrochemical effect of acid functionalisation of carbon nanotubes to be used in sensors development, Surface Science 605 (2011) 435-440.

[13] J. Yang, K. Ni, D. Wei, Y. Ren, One-step purification and immobilization of his-tagged protein via Ni2+-functionalized Fe3O4@ polydopamine magnetic nanoparticles, Biotechnology and bioprocess engineering 20 (2015) 901-907.

[14] J. Safari, S. Gandomi-Ravandi, Carbon nanotubes supported by titanium dioxide nanoparticles as recyclable and green catalyst for mild synthesis of dihydropyrimidinones/thiones, Journal of Molecular Structure 1065 (2014) 241-247.

[15] S. Liu, K. Yao, L.-H. Fu, M.-G. Ma, Selective synthesis of Fe 3 O 4, γ-Fe 2 O 3, and α-Fe 2 O 3 using cellulose-based composites as precursors, RSC Advances 6 (2016) 2135-2140.

[16] Y. Yu, C.Y. Jimmy, J.-G. Yu, Y.-C. Kwok, Y.-K. Che, J.-C. Zhao, L. Ding, W.-K. Ge, P.-K. Wong, Enhancement of photocatalytic activity of mesoporous TiO 2 by using carbon nanotubes, Applied Catalysis A: General 289 (2005) 186-196.

[17] V. Gupta, T.A. Saleh, Syntheses of carbon nanotube-metal oxides composites; adsorption and photo-degradation, Carbon Nanotubes-From Research to Applications, InTech2011.

[18] M. Baro, P. Nayak, T.T. Baby, S. Ramaprabhu, Green approach for the large-scale synthesis of metal/metal oxide nanoparticle decorated multiwalled carbon nanotubes, Journal of Materials Chemistry A 1 (2013) 482-486.

[19] Y. Lin, D.W. Baggett, J.-W. Kim, E.J. Siochi, J.W. Connell, Instantaneous formation of metal and metal oxide nanoparticles on carbon nanotubes and graphene via solvent-free microwave heating, ACS applied materials & interfaces 3 (2011) 1652-1664.

[20] P. Falaras, A. Hugot-Le Goff, M. Bernard, A. Xagas, Characterization by resonance Raman spectroscopy of sol–gel TiO 2 films sensitized by the Ru (PPh 3) 2 (dcbipy) Cl 2 complex for solar cells application, Solar energy materials and solar cells 64 (2000) 167-184.

[21] G.S. Gund, D.P. Dubal, N.R. Chodankar, J.Y. Cho, P. Gomez-Romero, C. Park, C.D. Lokhande, Low-cost flexible supercapacitors with high-energy density based on nanostructured MnO2 and Fe2O3 thin films directly fabricated onto stainless steel, Scientific reports 5 (2015).

[22] M.E.A. Warwick, K. Kaunisto, D. Barreca, G. Carraro, A. Gasparotto, C. Maccato, E. Bontempi, C. Sada, T.-P. Ruoko, S. Turner, Vapor phase processing of α-Fe2O3 photoelectrodes for water splitting: an insight into the structure/property interplay, ACS applied materials & interfaces 7 (2015) 8667-8676.

[23] H. Wu, G. Wu, L. Wang, Peculiar porous α-Fe 2 O 3, γ-Fe 2 O 3 and Fe 3 O 4 nanospheres: facile synthesis and electromagnetic properties, Powder Technology 269 (2015) 443-451.

[24] V.B. Koli, A.G. Dhodamani, S.D. Delekar, S.H. Pawar, In situ sol-gel synthesis of anatase TiO 2-MWCNTs nanocomposites and their photocatalytic applications, Journal of Photochemistry and Photobiology A: Chemistry 333 (2017) 40-48.

[25] N. Reddy, P. Bera, V.R. Reddy, N. Sridhara, A. Dey, C. Anandan, A.K. Sharma, XPS study of sputtered alumina thin films, Ceramics International 40 (2014) 11099-11107.

[26] M. Rehan, H.M. Mashaly, S. Mowafi, A.A. El-Kheir, H.E. Emam, Multi-functional textile design using in-situ Ag NPs incorporation into natural fabric matrix, Dyes and Pigments 118 (2015) 9-17.

[27] R.S. Amais, J.S. Ribeiro, M.G. Segatelli, I.V. Yoshida, P.O. Luccas, C.R. Tarley, Assessment of nanocomposite alumina supported on multi-wall carbon nanotubes as sorbent for on-line nickel preconcentration in water samples, Separation and Purification Technology 58 (2007) 122-128.

[28] F. Alimohammadi, M.P. Gashti, A. Shamei, A. Kiumarsi, Deposition of silver nanoparticles on carbon nanotube by chemical reduction method: Evaluation of surface, thermal and optical properties, Superlattices and Microstructures 52 (2012) 50-62.

[29] A.S. Subramanian, J.N. Tey, L. Zhang, B.H. Ng, S. Roy, J. Wei, Synergistic bond strengthening in epoxy adhesives using polydopamine/MWCNT hybrids, Polymer 82 (2016) 285-294.

[30] Y. Hu, C. Guo, Carbon nanotubes and carbon nanotubes/metal oxide heterostructures: synthesis, characterization and electrochemical property, Carbon Nanotubes-Growth and Applications, InTech2011.

[31] Y. Yu, J.G. Shapter, R. Popelka-Filcoff, J.W. Bennett, A.V. Ellis, Copper removal using bio-inspired polydopamine coated natural zeolites, Journal of hazardous materials 273 (2014) 174-182.

[32] P.G. Ingole, W. Choi, K.H. Kim, C.H. Park, W.K. Choi, H.K. Lee, Synthesis, characterization and surface modification of PES hollow fiber membrane support with polydopamine and thin film composite for energy generation, Chemical Engineering Journal 243 (2014) 137-146.

[33] M.-B. Wu, Y. Lv, H.-C. Yang, L.-F. Liu, X. Zhang, Z.-K. Xu, Thin film composite membranes combining carbon nanotube intermediate layer and microfiltration support for high nanofiltration performances, Journal of Membrane Science 515 (2016) 238-244.

[34] E.-S. Kim, B. Deng, Fabrication of polyamide thin-film nano-composite (PA-TFN) membrane with hydrophilized ordered mesoporous carbon (H-OMC) for water purifications, Journal of membrane science 375 (2011) 46-54.

[35] R. Du, J. Zhao, Properties of poly (N, N-dimethylaminoethyl methacrylate)/polysulfone positively charged composite nanofiltration membrane, Journal of membrane science 239 (2004) 183-188.